Theoretical and Applied Fracture Mechanics 143 (2026) 105489

Contents lists available at ScienceDirect

Theoretical and Applied Fracture Mechanics

journal homepage: www.elsevier.com/locate/tafmec

Advanced crack tip stress analysis using interaction integrals in high-resolution digital image correlation fields

Florian Paysan *, David Melching, Eric Breitbarth

German Aerospace Center (DLR), Institute of Materials Research, Linder Hoehe, 51147 Cologne, Germany

ARTICLE INFO

Keywords:
High-resolution digital image correlation
Finite element simulation
Interaction integral

ABSTRACT

The link between microscopic mechanisms and macroscopic behaviour, represented by the $da/dN-\Delta K$ curve, plays an increasingly important role in relating the fatigue crack growth curve required for component design to the underlying physics. High-resolution digital image correlation (HR-DIC) allows for in-depth analysis of microscopic fatigue crack growth mechanisms, but is rarely used to determine the SIF of the crack tip. This paper examines the applicability of the interaction integral in HR-DIC data and identifies factors that should be considered when evaluating the integral results.

A major influence is the integration near the PZ, which leads to an erroneous increase in the calculated SIF result. In addition, the large integration path gaps required in HR-DIC around the crack path significantly hinder accurate results. The effect of the crack face contact is overall small. While it slightly increases the SIF result, it does not correlate with the crack opening load K_{op}.

1. Introduction

The primary cause of structural failure in aircraft components is the formation of fatigue cracks due to non-constant multi-axial loading [1]. In materials science, fatigue crack growth is driven by the interaction of damaging and protective mechanisms near the crack tip [2]. Despite extensive research, mechanisms like crack closure, branching, or deflection, and their effects on crack propagation, such as crack tip stress, remain poorly understood [3]. The challenge lies in experimentally identifying these mechanisms, as they operate at the microscopic level and are often undetectable through post-mortem fracture surface analysis. Thus, high-resolution time-series imaging of the crack tip region is essential throughout the fatigue crack growth process [4].

Special focus is given to the examination of the plastic zone (PZ), including both primary and cyclic PZ, as it is not only the site of damaging crack propagation mechanisms, but also because its dimensions and shape reflect the prevailing stress state at the crack tip. Due to experimental limitations, the PZ has been subject of various 2D and 3D finite element simulations [5–9], which found that the shape of the PZ deviates from the dog-bone model, initially proposed by Dugdale [10]. *Besel et al.* [11] observed that the shape of the PZ underwent changes at both the free surface and within the volume of the specimen. They attributed these observations to the interaction between the plane strain within the volume and the plane stress at the surface of the specimen. Both conditions depend strongly on the specimen thickness and the maximum crack tip stress [12,13]. In recent years, the advent of high-resolution digital image correlation (HR-DIC) has notably increased the number of experimental studies examining the PZ. In 2013, HR-DIC research was conducted by *Carroll et al.* [14]. They analyse the dislocation structures in the plasticized region in proximity to the crack tip. It was observed that the accumulation of local strains within both the PZ and the plastic wake is highly inhomogeneous. Other studies used HR-DIC to examine the wing shape of the PZ. *Zhang et al.* [15] examined the effects of overload on the PZ and found that the subsequent deformation zone was significantly smaller. A comparable investigation of the PZ following an overload was conducted by *Vasco-Olmo et al.* [16]. The results agreed with those of *Zhang et al.* [15], indicating that the temporary delay in crack growth rate was significantly associated with the overload-induced PZ. *Besel et al.* [11] concentrated on examining the shape of the PZ in relation to varying sheet thicknesses and crack tip stresses. Their findings elucidated a clear correlation between the PZ geometry and the sheet thickness supporting their numerical studies.

Digital image correlation (DIC) has become a crucial tool in fracture mechanics, as it allows to determine crack tip stresses based on measured full-field displacement data near the crack tip, thereby providing valuable insights into the mechanics of fracture. The stress is usually derived from the measured strains by a known constitutive law (e.g. Hooke's law). The currently applied methods to calculate stress tip field descriptors like SIFs or T-stress can be grouped into two classes

* Corresponding author.
E-mail address: Florian.Paysan@dlr.de (F. Paysan).

https://doi.org/10.1016/j.tafmec.2026.105489
Received 22 December 2025; Received in revised form 26 January 2026; Accepted 29 January 2026
Available online 5 February 2026
0167-8442/© 2026 The Author(s). Published by Elsevier Ltd. This is an open access article under the CC BY license (http://creativecommons.org/licenses/by/4.0/).

— invariant integrals and over-deterministic methods. Both require an accurate determination of the crack tip position. While *Gehri* [17] uses the displacements of the two crack flanks as the basis for evaluation, *Rethore* [18] derived an iterative correction formula to refine the crack tip position of a mode I crack based on an initial estimate and the over-deterministic method. *Melching et al.* [19] used physical deep symbolic regression to find more general iterative correction formulas for mode II and mode-I-dominated mixed mode loading scenarios. Furthermore, *Strohmann et al.* [20] employ a convolutional neural network for crack tip detection in noisy DIC data and *Melching et al.* [21] improved upon this by using explainable machine learning to select a model which focuses neural attention on the crack tip field. While these approaches have primarily been applied under standard conditions, extreme environments, such as high temperatures, pose significant additional challenges due to heat-induced air flow and illumination variations [22,23]. Zheng et al. [24] addressed this by combining the DIC displacement field with the Williams model to automatically and accurately determine the crack tip position under such demanding conditions.

For the purpose of calculating crack tip stresses from DIC data, the J-integral has become particularly well-established [25–27]. Given the complex cyclic behaviour of the material within the PZ, all studies have in common that integration paths are placed outside the PZ, justifying the use of Hooke's law as the material model for the J-integral formulation. *Gonzales et al.* [25] calculate SIFs during an overload for different integration path geometries. Although their integration paths contain gaps to exclude the erroneous singular strain surrounding the crack path, their K_{I} results converge. *Breitbarth et al.* [26] recommend using multiple integration paths to negate the impact of DIC noise. Additionally, they assert that the J-integral does not require an exact crack tip position. *Molteno et al.* [27] introduces a new decomposition method to extract mixed-mode SIFs from the classical J-integral calculation. He investigates different integration paths with radii ranging from r = 3 mm to r = 12 mm. He found that the $K_{\mathrm{I-III}}$-results start to converge from r > 4 mm. The interaction integral itself belongs to the methods of linear-elastic fracture mechanics and has been successfully employed to DIC data to calculate mixed-mode SIFs [26,28]. In his studies, *Breitbarth et al.* [26] conclude that DIC noise has a more significant role in determining the final results than inaccuracies regarding the position of the crack tip. *Rethore et al.* [28] propose that the interaction integral should be evaluated as a domain integral, which has the advantage of reducing sensitivity to errors made by the DIC displacement calculation.

However, in all studies mentioned above macroscopic DIC data is used, which does not permit an in-depth analysis of local fatigue crack growth mechanisms as is possible with HR-DIC data. Due to the large distance between the crack tip and the integration contours or paths, respectively, effects such as plasticity of the PZ and plastic wake, as well as crack closure contact, are neglected in macroscopic DIC.

The objective of this paper is to investigate the impact of near-crack-tip effects on SIF results calculated by the interaction integral method using a linear-elastic line integral formulation assuming small-scale-yielding-conditions. Therefore, the interaction integral results obtained from experimental HR-DIC data are compared to those from numerical FE simulations, in order to systematically identify the underlying causes of the observed effects. Although the line integral is evaluated in close proximity to the crack tip, a purely linear-elastic formulation is employed. This choice substantially reduces the evaluation effort, as the highly complex, locally varying cyclic stress–strain behaviour in the near-tip region is difficult to capture reliably using constitutive material models. The FE simulations provide a controlled framework in which individual influencing factors can be isolated and analysed independently. If similar characteristics are observed in both the FE-based and HR-DIC-based line integral evaluations, it can be inferred that the corresponding prescribed influence in the simulation is also a plausible cause of the behaviour observed in the experimental data.

In particular, this paper investigates the following potential influencing factors:

- Given the limited measurement range of HR-DIC systems, this study examines the impact of the near-PZ on the outcome of SIF calculations based on linear-elastic interaction integrals and small-scale yielding conditions (SSY).
- The share of the gab of the entire integration path in HR-DIC evaluations is considerably larger than to those commonly used in macroscopic DIC evaluations. This study looks at how the gap affects the SIF result and the impact of integrating parts of the path within the plastic wake.
- Finally, it is examined how the SIF result of the interaction integral reflects the crack face contact due to crack closure.

In this study, fatigue crack propagation experiments are performed on a 2 mm thick MT-160 specimen (aluminium alloy AA2024-T3, widely used in the aircraft industry). HR-DIC measurements are performed throughout the entire fatigue crack growth. To illustrate the data sets, Fig. 1 presents a comparison between two different strain fields: a macroscopic DIC strain field, commonly used to determine SIFs through line integrals, and a high-resolution DIC (HR-DIC) strain field. The FE model that serves for comparison is based on the same MT-160 geometry and copies the boundary and loading constraints.

2. Methodology

2.1. Interaction integral

In order to distinguish between mode-I and mode-II crack loading conditions, *Stern et al.* [30] and *Yau et al.* [31] developed the so-called interaction integral $J^{(a,b)}$, based on the classical J-integral implementation. The mathematical definition of the interaction integral is given in Formula (1). For the present analysis, a plane stress state is assumed, with purely linear-elastic material behaviour. The integral evaluates the stresses σ, strains ε, and displacements u along an integration path Γ_r. n defines the outward unit normal to the integration path Γ_r. In general, the interaction integral is based on the superposition of two loading cases $^{(1)}$ and $^{(2)}$, where in practice (1) is the actual measured field and (2) is an arbitrary auxiliary field.

$$J^{(1,2)} = \lim_{r\to 0}\int_{\Gamma_r}\left[\sigma^{(2)}_{mn}\varepsilon^{(1)}_{mn}\delta_{1j} - \left(\sigma^{(1)}_{ij}u^{(2)}_{i,1} - \sigma^{(2)}_{ij}u^{(1)}_{i,1}\right)\right] n_j \,\mathrm{d}s \tag{1}$$

More precisely, two different auxiliary fields $^{(2a)}$ and $^{(2b)}$ are defined. The resulting system of equations allows to determine $K_{\mathrm{I}}^{(1)}$ and $K_{\mathrm{II}}^{(1)}$:

$$\begin{aligned}
K_{\mathrm{I}}^{(1)} &= \frac{E}{K^2}\cdot\left[K_{\mathrm{II}}^{(2\mathrm{a})}\cdot J^{(1,2\mathrm{b})} - K_{\mathrm{II}}^{(2\mathrm{b})}\cdot J^{(1,2\mathrm{a})}\right]\\
K_{\mathrm{II}}^{(1)} &= \frac{E}{K^2}\cdot\left[K_{\mathrm{I}}^{(2\mathrm{b})}\cdot J^{(1,2\mathrm{a})} - K_{\mathrm{I}}^{(2\mathrm{a})}\cdot J^{(1,2\mathrm{b})}\right]\\
K^2 &= K_{\mathrm{I}}^{(2\mathrm{b})}\cdot K_{\mathrm{II}}^{(2\mathrm{a})} - K_{\mathrm{I}}^{(2\mathrm{a})}\cdot K_{\mathrm{II}}^{(2\mathrm{b})}
\end{aligned}\tag{2}$$

If a pure mode-I loading is used for the auxiliary field $^{(2a)}$ or a mode-II crack loading is used for the auxiliary field $^{(2b)}$, the above equations simplify as follows:

$$\begin{aligned}
K_{\mathrm{I}}^{(1)} &= \frac{E}{K_{\mathrm{I}}^{(2\mathrm{a})}}\cdot J^{(1,2\mathrm{a})}\\
K_{\mathrm{II}}^{(1)} &= \frac{E}{K_{\mathrm{II}}^{(2\mathrm{b})}}\cdot J^{(1,2\mathrm{b})}
\end{aligned}\tag{3}$$

DIC measurements only provide the displacement and total strain field as its derivative of the free surface of the MT-160 specimen. In order to calculate the stresses σ in Eq. (1), a constitutive equation that connects stresses to strains is needed. The local cyclic stress–strain behaviour within the PZ is complex. An incorrect representation of stress–strain behaviour may result in the loss of path independence of the interaction integral as has been demonstrated in case of the J-integral [32]. Consequently, the integration path is positioned outside the PZ within the linear-elastic crack tip field (see Fig. 2), thus justifying the usage of Hooke's linear-elastic constitutive law. Unfortunately, plastic wake, inaccurate strain calculations and scatter around the

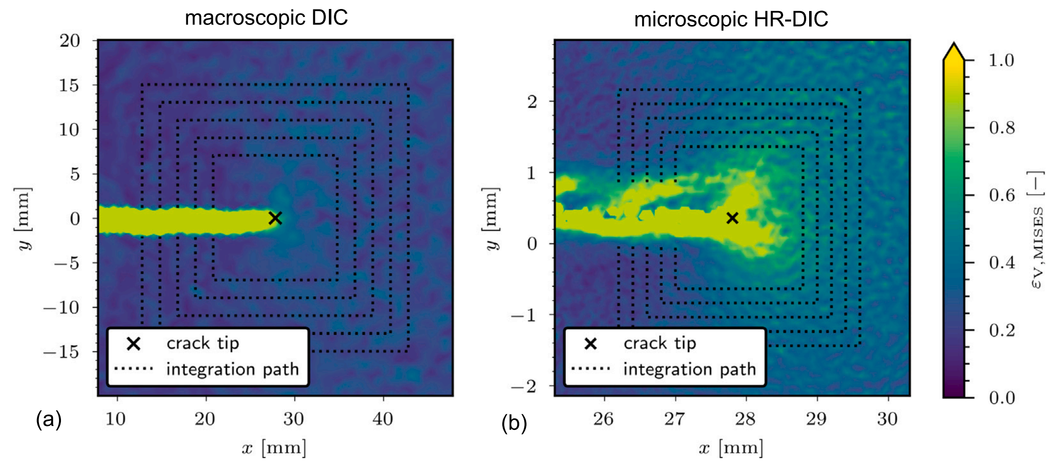

Fig. 1. Comparison of (macroscopic) DIC and HR-DIC strain fields showing the equivalent MISES strain: (a) a macroscopic DIC strain field obtained from a 3D measurement and (b) an HR-DIC strain field captured using an optical microscope; both evaluated at $K_{\mathrm{norm}} = 14.9\,\mathrm{MPa}\sqrt{\mathrm{m}}$ (maximum load) and $a = 27.8\,\mathrm{mm}$; K_{norm} is determined by ASTM E647-15 [29] (see Eq. (4)).

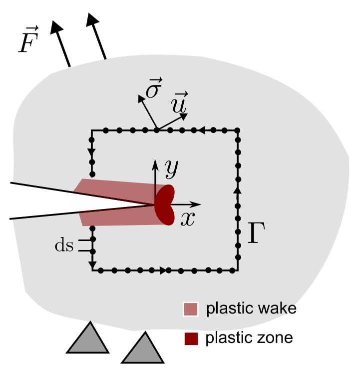

Fig. 2. Integration path definition for evaluating the interaction integral in displacement field data; the definition is equivalent to the implementation in *CrackPy* [33].

crack path hinder to close the integration paths. While this gap can be neglected for most cases in macroscopic DIC [25], its influence for HR-DIC data needs to be considered.

In this paper, the authors follow the methodology from *Breitbarth et al.* [26] to evaluate the interaction integral with DIC displacement field data. The algorithm is implemented in the open-source software package *CrackPy* (https://github.com/dlr-wf/crackpy), a crack analysis tool written in Python, which offers several methods for crack tip stress field evaluation. The website also offers the code of the routine to evaluate the interaction integral on DIC data used for this study. The sequence of steps in the numerical evaluation is as follows:

1. A rectangular integration path is defined manually outside the plastic zone and discretized into individual integration points, as schematically illustrated in Fig. 2. In the present study, the spacing between adjacent integration points is constant to $0.05\,\mathrm{mm}$, corresponding to the refined element size used in the FE simulations and approximately matching the spacing between individual facets in the 2D HR-DIC displacement field grid. The integration path contains a gap that excludes the crack path and plastic wake.
2. At each integration point, the displacement vector u is obtained by linear interpolation from the nearest Gauss points in the FE simulations or from the neighbouring facets in the HR-DIC data. Based on the displacement field, the strain tensor ε is computed as its spatial derivative. Since the integration path is located outside the elastic–plastic deformation zone, purely linear-elastic material behaviour can be assumed. Consequently, the stress tensor is determined using Hooke's law for plane stress conditions.
3. In the next step, the interaction integral is evaluated. As the auxiliary field $^{(2)}$, the Williams series expansion is employed, retaining only the first positive term. The interaction integral is then computed using numerical trapezoidal integration. Here, the integration path gap is skipped.
   To evaluate K_{I} and K_{II} separately, two auxiliary loading cases are considered: auxiliary field $^{(2a)}$ corresponds to pure mode I loading ($K_{\mathrm{I}} = 1\,\mathrm{MPa}\sqrt{\mathrm{m}}$), whereas auxiliary field $^{(2b)}$ represents pure mode-II loading ($K_{\mathrm{II}} = 1\,\mathrm{MPa}\sqrt{\mathrm{m}}$). Finally, the stress intensity factors are determined using Eq. (3).

In the context of DIC data, it is recommended to use multiple integration paths to mitigate the impact of inherent data noise on the integral results.

2.2. Finite element model

All simulations are conducted using ANSYS Mechanical APDL on a RedHat Linux workstation with dual Intel Xeon Gold 6240 18C CPUs and 256 GB DDR4-2933 RAM. The numerical simulations are based on the FE model from [34]. For completeness, a brief summary of the FE model is provided below:

The FE model is derived from the MT-160 specimen geometry and its general dimensions are displayed in Fig. 3a. To optimize computational efficiency, a 1/8 symmetry 3D model is used, excluding the clamping region and holes to enable mapped meshing. As illustrated in Fig. 3a, the front view of the model depicts a quarter of the entire area of the MT-160 specimen. Furthermore, the model is halved in the thickness direction, resulting in a 1/8 model. The models constraints are defined in the following way: The load F is applied through a pilot node coupled to all top surface nodes. Symmetry planes restrict node movement perpendicular to their planes, with a crack of length a defined at the model's bottom. Symmetry constraints in the interval $x \in [0, a]$ are removed to allow crack surface deformation.

The model uses a mapped mesh strategy with 8-node linear hexahedron SOLID185 elements. Fig. 3c shows the mesh used near the crack tip. The structured mesh is divided into three sections: a global mesh, a refined region near a for detailed analysis, and a transition section connecting both. The dimensions of the refined region depends on the initial PZ size estimate according to Irwin r_p. The refined region has elements with an aspect ratio of 1 and an element size of $0.05\,\mathrm{mm}$ in all three Cartesian directions. This means that the elements have a cuboid shape. In order to achieve more precise results, particularly

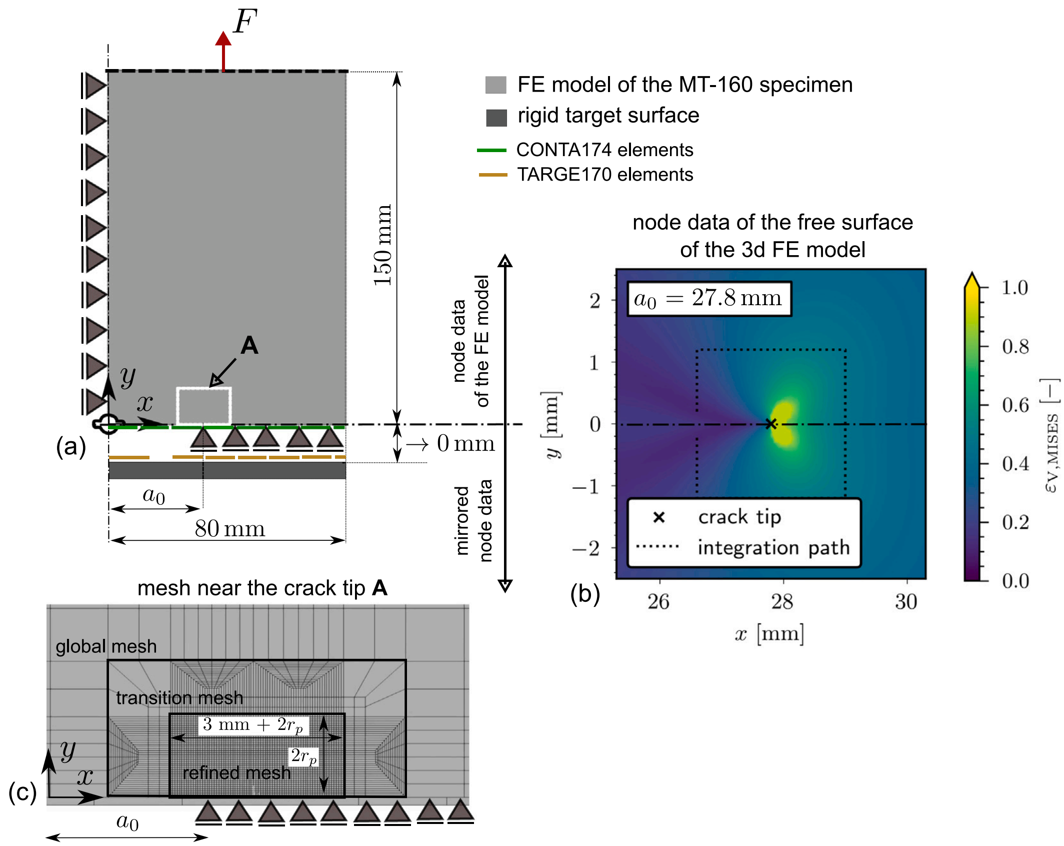

Fig. 3. Strategy to evaluate the interaction integral on numerical displacement field data: (a) 1/8 FE model of a MT-160 specimen including its constraints and contact element definition, (b) the displacement node data, partially mirrored, of the free specimen surface and (c) the mesh used near the crack tip position.

in the context of crack closure analysis, it would be preferable to employ a reduced element size. However, the utilization of smaller elements in combination with the contact definition, as will be subsequently outlined, can result in issues related to solution convergence, attributable to substantial element distortions near the crack plane. The size of the transition zone is automatically determined by the size of the refined area, in order to ensure the generation of high element quality. Outside the refined section, a flexible element size of 0.5 mm is used. The contact formulation needed is defined via asymmetric contact elements (provided by ANSYS Mechanical APDL), neglecting surface effects like crack surface roughness. A rigid target plate (SOLID185, element size: 1 mm) is defined for the MT-160 model, with frictionless rigid-to-flexible contact set between the MT-160 model and the rigid target surface. The rigid-target-surface works as counter-plate for the free-deformable crack surface of the MT model. The crack surface uses CONTA174 overlaying the bottom surface of the MT-160 FE model and TARGE170 elements on top of the rigid target surface. The Augmented Lagrange Algorithm serves as the contact solver, with contact stiffness 1 N/mm^2 and penetration limit 1 μm to minimize penetration. All initial gaps are closed. To analyse the impact of the near-PZ integration, the FE model can include both linear-elastic and elastic–plastic material behaviour using bilinear isotropic hardening, based on the properties of AA2024-T3. The material properties, used for the material model, are given in Table 1.

In order to separate the effects of PZ and plastic wake, the authors perform both simulations with and without crack propagation (see Fig. 4). In the latter case, the crack length remains constant throughout the entire simulation, i.e., no crack growth occurs (see Fig. 4a). This approach offers several advantages: both the primary PZ and the cyclic PZ can be resolved. This method bases on the assumption that crack growth is negligibly small. All simulations without crack propagation include a total of ten loading cycles, each consisting of a loading and unloading step. The maximum load and load ratio are set to F_{max} = 15 kN and $R = 0.1$ comparable to the fatigue crack growth experiments in Section 2.3 below. This study implements the Releasing-Constraint Method for conducting crack propagation within the FE simulation. For each loading cycle, an additional step is added where the boundary conditions of an element row ahead of the current crack front in the crack plane are released. Thus, the crack grows by one element length per cycle. The principle is schematically shown in Fig. 4b. Between crack growth steps, the crack is subjected to only one loading and unloading sequence, despite literature [36–38] recommending at least two cycles. This choice aims to save computation time as is not the focus of this paper to determine accurate crack opening SIFs (K_{op}), supported by *Camas et al.* [39,40], who assessed the impact as being negligible. The crack propagation is performed within the refined element region. The boundary conditions are released at minimum load F_{min}, referencing Laird's [41] observations of crack tip blunting at minimum load. A total of 40 loading cycles (150 steps) are simulated, resulting in a crack length of a_{Rifo} = 2 mm. That means that the starting crack length is $a - a_{Rifo}$. As has been already mentioned, it is important to note that not every FE simulation within the discussion section are performed in the same way, i.e. some do not include crack propagation and a contact definition, while others do. The configuration information used is given in the corresponding discussion section separately.

Table 1
Material properties of AA2024-T3, taken from [35].

Young's Modulus	E	68 000 MPa
Poisson's Ratio	ν	0.33
Yield Strength	$R_{p0.2}$	345 MPa
Tangent Modulus	m_t	984 MPa

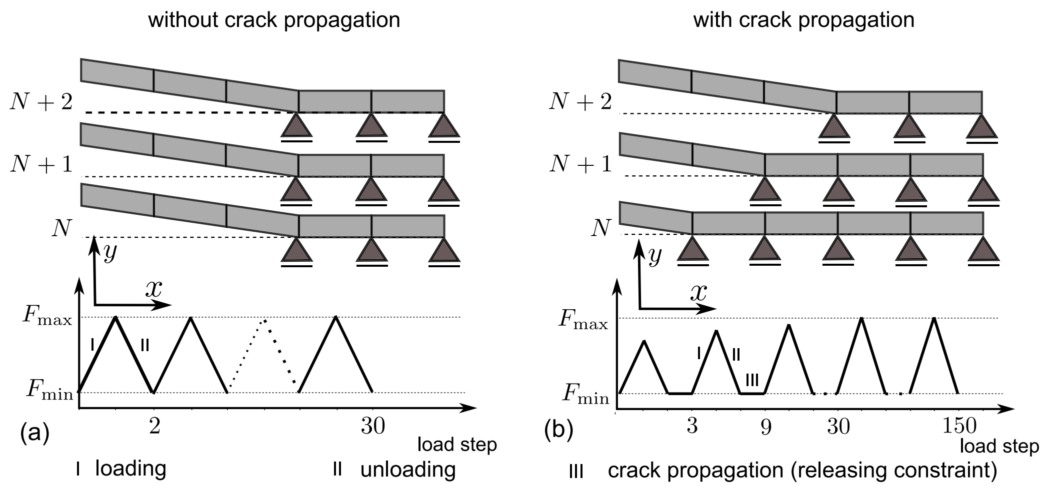

Fig. 4. Simulation procedures to analyse the PZ, the plastic wake and crack closure: (a) loading sequence without crack propagation and (b) loading sequence with crack propagation according to the releasing-constraint method.

In order to evaluate the interaction integral in a comparable way to the evaluation in HR-DIC data, the nodal displacement data on the free surface of the FE simulation is extracted. In the FE model, only the displacements above the crack are calculated. Consequently, the nodal displacements are symmetrically mirrored to the crack's underside, with the crack itself serving as the mirror axis. The procedure is schematically illustrated in Fig. 3. Both the node data above the crack and mirrored one are the input for interaction integral evaluation following the explanations in Section 2.1.

Table 2
Resolution and facet settings for DIC evaluation of the 3D DIC and 2D HR-DIC measurement systems.

Parameter	3D DIC System	2D HR-DIC System
Measurement area	330 mm x 160 mm	10.2 mm x 5.4 mm
Facet spacing	16 pixels x 16 pixels	30 pixels x 30 pixels
Facet size	21 pixels x 21 pixels	40 pixels x 40 pixels
Spatial resolution	0.59 mm/facet	47 μm/facet

2.3. Fatigue crack growth experiments

A fatigue crack growth experiment was conducted as a comparison to the FE results on a 2-mm-thick MT-160 specimen produced from AA2024-T3. The fatigue crack propagates vertical the rolling direction of the sheet material (L-T crack orientation). The SIF behaviour of a mode-I fatigue crack can be expressed by the following Formula that refers to ASTM E647-15 [29]:

$$K_{\text{norm}} = \frac{F}{t}\sqrt{\frac{\pi\alpha}{2W}\sec\left(\frac{\pi\alpha}{2}\right)} \tag{4}$$

α denotes the ratio of crack length a and the specimen width W. The experimental setup is illustrated in Fig. 5a, utilizing a servo-hydraulic testing machine to apply sinusoidal loading with a constant amplitude. The load parameters are consistent with the numerical studies, with $F_{\max} = 15\,\text{kN}$ and $R = 0.1$. The test stand is equipped with a robot-assisted HR-DIC system (Fig. 5a) [42]. This system features a KUKA iiwa robot that moves a Zeiss 206C stereo microscope, equipped with a Basler a2A5320-23umPro global shutter 16-megapixel CMOS camera, allowing for HR-DIC displacement field measurements around the crack tip during crack propagation. A detailed overview of the setup, including robotic algorithms for optimizing image quality is provided in [42].

Prior to the fatigue crack growth experiment, the robot moves the microscope to all predefined positions on the specimen surface where the crack is expected to propagate. The area is covered in a checkerboard pattern at zero load, and a reference image is captured at each position. Automatic algorithms ensure precise alignment of the optical camera system with the specimen surface, as well as optimal sharpness and contrast of the images. These algorithms minimize DIC noise caused by poor image quality. After this calibration phase, the crack propagation phase begins. Crack growth starts from a milled initial notch in the centre of the MT-160 specimen with an initial crack length of 5 mm. The specimen is cyclically loaded until a crack length increment of $\Delta a = 0.5\,\text{mm}$ is measured using a direct current potential drop (DCPD) system ($I = 100\,\text{mA}, U = 60\,\text{mV}$). The system then pauses, and the robot moves to the reference position that best captures the crack tip area. In the following an image at maximum and minimum load is taken (see Fig. 5b). This sequence is repeated every $\Delta a = 0.5\,\text{mm}$. Once this sequence repeated 20 times, such that a crack length increment of $\Delta a = 10\,\text{mm}$ has been achieved, an entire loading step is captured by in total 30 load levels at which an image is captured. This is required in order to analyse the influence of crack closure on the results of the interaction integral. As with the previous sequence, this sequence is repeated until final failure of the MT-160 specimen. In addition to the robot-assisted HR-DIC system on the front side of the specimen, a 3D DIC system is located on the backside, enabling to capture displacement fields at the macroscopic level. Here, a GOM Aramis 12M 3D DIC System is used. The 3D DIC system consists of two individual 12-megapixel cameras with a distance of 98 mm and angles 25° relative to each other. The measurement volume is set to $200\,\text{mm} \times 150\,\text{mm} \times 21\,\text{mm}$. The settings for the DIC evaluation and the corresponding resolutions of the 3D DIC and 2D HR-DIC systems are provided in Table 2. The DIC evaluation is performed using the licensed Zeiss GOM Aramis 2020 software [43].

The fatigue crack growth experiment was conducted entirely under small-scale yielding (SSY) conditions. The validity criterion $(W - a) \geq 1.25F_{\max}/(B\sigma_y)$ [29] is satisfied for crack lengths up to $a = 67\,\text{mm}$. As specimen failure occurred at $a = 62\,\text{mm}$, the condition was therefore met throughout the test.

3. Results and discussion

The objective of this study is to identify the characteristics that must be considered when applying the interaction integral to HR-DIC data. To ensure that the identified phenomena not only account for a single data point, the authors first investigate the determined SIF results along the entire fatigue crack. Subsequently, it is attempted to separate the individual systematic effects by comparing the HR-DIC result with numerical results at a crack length of $a = 27.8\,\text{mm}$ using this data point as a reference being exemplary for all.

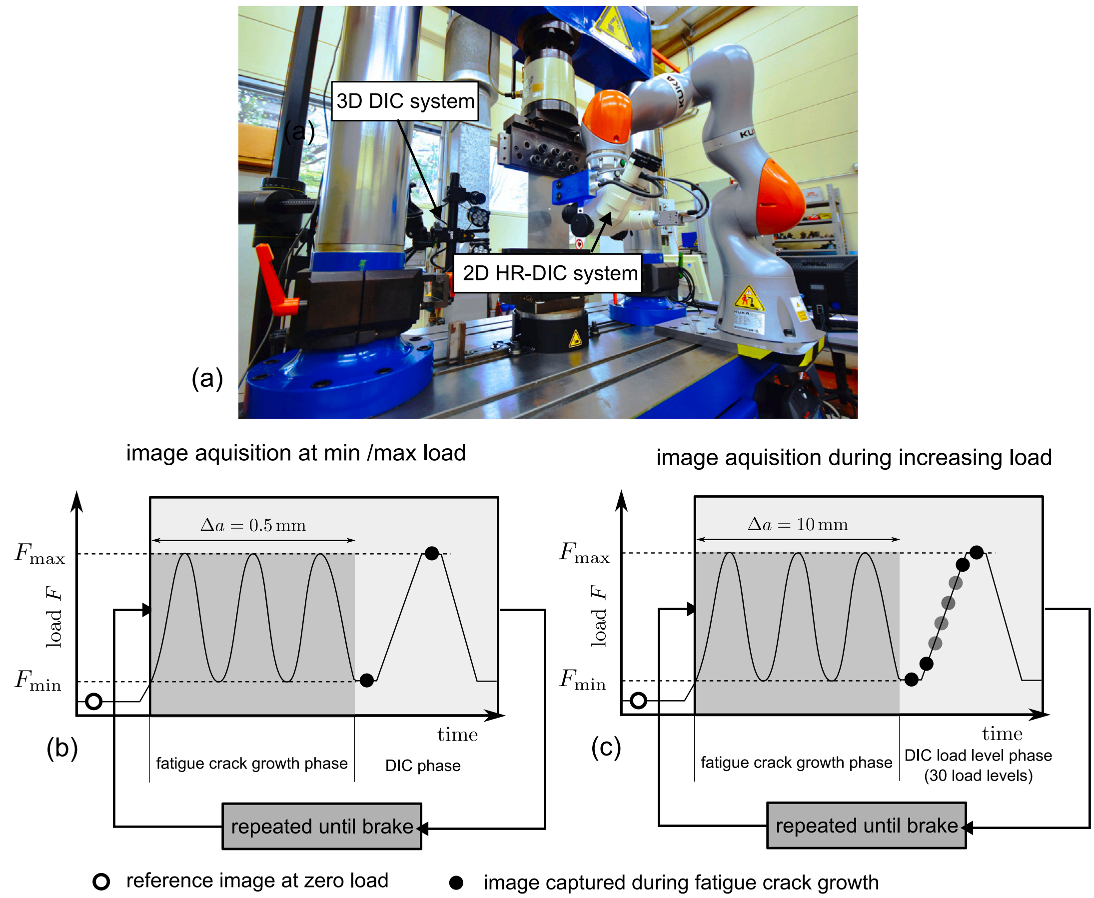

Fig. 5. Fatigue crack growth experiments on MT-160 specimens of AA2024-T3 with multi-scale DIC measurements: (a) Experimental setup in the laboratory, (b) measurement sequence every $\Delta a = 0.5$ mm, (c) measurement sequence every $\Delta a = 10$ mm; at each image trigger point both backside DIC and the HR-DIC system are activated.

3.1. Fatigue crack growth curve and crack tip stresses

In general, within this section, two different kinds of crack propagation curves are distinguished: $da/dN - \Delta K$-curves according to ASTM E647-15 [29] and $da/dN - \Delta K_{\mathrm{DIC}}$-curves that are constructed based on DIC and HR-DIC data. The following two paragraphs provide an overview over their construction procedures.

Crack propagation curve according to ASTM E647-15
The crack length is determined through potential drop measurements, and the crack growth rate is assessed using the secant method with crack growth intervals of $\Delta a = 0.1$ mm. From the use of potential drop measurement follows that both crack tips (left and right in regards to the centre notch) are taken into account for the crack length determination. A separate analysis of each side is not possible and the crack is assumed to grow straight. Finally, K_{norm} is computed according to Eq. (4).

DIC and HR-DIC crack propagation curves
Fig. 6 presents the crack growth curves obtained from DIC and HR-DIC measurements. Images at maximum and minimum load levels were captured at intervals of 0.5 mm. The displacement field data at both load levels were employed to calculate the crack tip SIFs, $K_{\mathrm{I,DIC}}$ and $K_{\mathrm{I,HR-DIC}}$, using the interaction integral method outlined in Section 2.1. The difference between these two values provides the cyclic SIF ΔK. For the determination of $K_{\mathrm{I,DIC}}$, 20 integration paths are evaluated. The closest path to the crack tip maintains an upper, lower, and lateral distance of 5 mm. The distance between subsequent paths is 1 mm, excluding the crack path itself. An example of the integration paths in the macroscopic DIC data is given in Fig. 1a. The definition of the integration paths in the HR-DIC data, as shown in Fig. 1b, is not fixed. Instead it is adjusted according to the dimensions of the PZ. The PZ is estimated by applying the yield stress as a threshold. An additional offset of 0.5 mm is applied, setting the minimum distance of the first integration path from the crack tip. The spacing between paths is 0.2 mm. The gap around the crack path in the integration paths is modified to account for the dimensions of the plastic wake. The median of the individual path results determines the final $K_{\mathrm{I,DIC}}$ or $K_{\mathrm{I,HR-DIC}}$ results. Crack growth rate measurements are based on crack length data obtained using the crack tip detection model ParallelNets [21], which is part of the CrackPy package [33]. Here, the displacement fields, u_x and u_y, are designated as inputs. These inputs are then processed by a trained U-Net neural network, which segments both the crack path and tip. To enhance the system's robustness, a fully-connected neural network is employed in parallel to further optimize the detection accuracy. Therefore, the crack lengths for both the DIC and HR-DIC curves are derived from the displacement field data. Crack lengths are smoothed using a moving average over three consecutive points, and the slope between three consecutive data points is calculated to determine the crack growth rate da/dN.

Fig. 6 shows the crack growth curves based on DIC and HR-DIC measurements as well as the FCP curve according to ASTM E647-15 [29].

From a methodology point of view, both different FCP curve types are difficult to compare since the FCP curves according to ASTM E647-15 [29] incorporates the growth rate of two crack tips, while the DIC

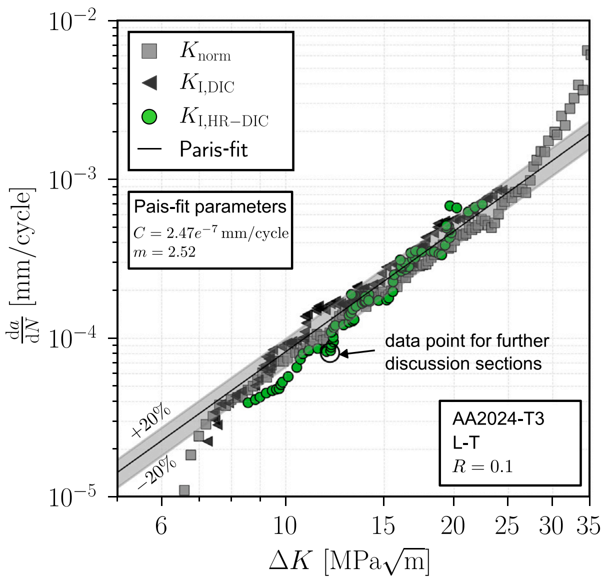

Fig. 6. Fatigue crack growth curve $da/dN - \Delta K$ evaluated according to ASTM E647-15 [29] and DIC and HR-DIC data; AA2024-T3 in L-T crack orientation at $R = 0.1$.

Table 3
Deviation analysis of the single FCP curves; determined against a Paris fit with $C = 2.47e^{-7}$ and $m = 2.52$ and evaluated within the SIF interval of $\Delta K = [8, 25]\,\mathrm{MPa}\sqrt{\mathrm{m}}$.

Curve type	R^2 [-]	Proportion outside the 20% scatter band [%]
ASTM curve	0.99	3%
DIC curve	0.98	5%
HR-DIC curve	0.96	17%

and HR-DIC based ones only consider the crack tip of the right side of the MT-160 specimen. Nevertheless, from a qualitative perspective, all curves shown in Fig. 6 reveal the linear behaviour on a double-logarithmic scale. This linearity confirms the applicability of the Paris law for describing the crack growth behaviour in all presented curves, as most sections of all curves fall within a common 20% scatter band that is often used as reproducible criterion for $da/dN - \Delta K$-curves of the same material. This shows the redundancy of the methods to each other. In order to assess the deviation of the curves in the Paris regime, all available data points (ASTM, DIC and HR-DIC) are used within the interval $8\,\mathrm{MPa}\sqrt{\mathrm{m}} < \Delta K < 25\,\mathrm{MPa}\sqrt{\mathrm{m}}$ for fitting the Paris law. The fit is illustrated in Fig. 6 and is defined by $C = 2.47e^{-7}$ and $m = 2.52$ as fitting parameters, resulting in the formula

$$\frac{da}{dN} = C\,(\Delta K)^m \quad \left[\Leftrightarrow \quad \log\left(\frac{da}{dN}\right) = \log(C) + m \cdot \log(\Delta K)\right]. \tag{5}$$

Those fitting parameters are consistent to literature values [44] for the L-T crack orientation of AA2024-T3. In the following, each curve is evaluated for its deviation against Eq. (5). The results are given in Table 3.

Generally, all fatigue crack propagation (FCP) curves show a good agreement with each other as quantified by the large R^2-values. While only a few data points of the ASTM and DIC FCP curves are located outside the 20% scatter band, this value is increased in case of the HR-DIC FCP curve. Comparing both the DIC and HR-DIC FCP curves, it can be recognized that the HR-DIC one always slightly shifted to the right, indicating that at larger cyclic crack tip stress lower growth rates would exist. Since the growth rates in DIC and HR-DIC are almost identical in double-logarithmic scale, this phenomenon mainly results from different measured SIF values as shown in Fig. 7.

Fig. 7 illustrates the variation of the measured $K_{I,DIC}$ and $K_{I,HR-DIC}$ results at maximum load F_{max} and minimum load F_{min} along the crack length a. The scatter bands in both graphs represent the maximum and minimum K_I values from the integration path results, indicating that the application of the interaction integral based on HR-DIC data results in a reduction in scatter of the path results compared to those derived from DIC data. Consequently, HR-DIC data not only enables the identification of microscopic effects in fatigue cracks but also its crack tip stress determination is less affected by the DIC measurement noise. Furthermore, Fig. 7 provides an explanation for the shift of HR-DIC FCP curves to the right compared to the DIC-based FCP curves. Fig. 7a illustrates that $K_{I,HR-DIC}$ at maximum load exceeds $K_{I,DIC}$ by 2 to $6\,\mathrm{MPa}\sqrt{\mathrm{m}}$. This results in a shift of the HR-DIC-based crack growth curves below the two remaining crack growth curves, particularly in the range $\Delta K \in [5, 15]\,\mathrm{MPa}\sqrt{\mathrm{m}}$. The subsequent sections analyse the reasons for the deviation of $K_{I,HR-DIC}$ compared to the other two curve trends and provide recommendations for the path definition for the application of the interaction integral in HR-DIC displacement field data.

3.2. The influence of integrating near the PZ

Due to the limited measurement range of HR-DIC systems, the integration paths for the interaction integral are in close proximity to the PZ. Since plastic deformation affects the crack tip field near the PZ, the behaviour deviates from pure linear-elastic conditions. In order to investigate the impact of integrating in close proximity to the PZ, the authors employ the FE model from Section 2.2. Here, no crack propagation is conducted during the load cycles. In regards to the material model implemented, both linear-elastic (elastic modulus $E = 73.1\,\mathrm{GPa}$, Poisson ratio $\nu = 0.33$) and a elastic–plastic material model are used separately. In the latter case, a bilinear isotropic hardening material model (yield stress $\sigma_{yield} = 350\,\mathrm{MPa}$, hardening modulus $m_t = 984\,\mathrm{MPa}$) is employed. To evaluate the influence of the PZ on K_I, a total number of 200 quadratic closed integration paths are analysed, starting at a distance of $r = 0.05\,\mathrm{mm}$ from the crack tip position. For each integration path r is increased by $\Delta r = 0.05\,\mathrm{mm}$. Consequently, the last integration path is located at $r = 10\,\mathrm{mm}$. Fig. 8 compares the K_I path results based on FE data $K_{I,FE}$ coming from elastic or elastic–plastic simulations with those results derived from HR-DIC displacement field data $K_{I,HR-DIC}$.

Figs. 8b and d illustrate the convergence behaviour of the path results based on FE and HR-DIC displacement field data for $K_{norm} = 14.9\,\mathrm{MPa}\sqrt{\mathrm{m}}$ as a function of the radius r. The von MISES equivalent strain fields are depicted in Figs. 8a and c. Within the PZ, the assumption of Hooke's law in the context of the interaction integral leads to an overestimation of K_I. The size of the PZ in both Figs. 8b and d is estimated using Irwins formula under plane stress condition $r_p = 0.36\,\mathrm{mm}$. This calculated SIF overestimation arises from the assumption of linear-elastic behaviour (Hooke's law) in the derivation of the interaction integral although the material within the PZ is elastic–plastic. As a result of the inaccurate description of the material behaviour, the integral becomes path-dependent, as also emphasized by *Xu et al.* [32,45]. Outside the PZ, in close proximity of the PZ, the material exhibits purely linear-elastic behaviour, enabling the application of the interaction integral. However, both convergence analyses shown in Figs. 8b and d reveal that the path results based on the elastic–plastic FE simulation $K_{I,FE}$ and HR-DIC data $K_{I,HR-DIC}$ do not converge immediately, even when the material behaviour should be adequately represented by Hooke's law. A transition region exists in which K_I is still larger than K_{norm}. This is attributed to deviations in the crack tip field due to the presence of the PZ, compared to the linear-elastic solution [46]. As the radius r increases, the influence of the PZ on the crack tip field diminishes, and the path results begin to converge. At a radius of $r = 1.4\,\mathrm{mm}$, the influence of the PZ on the crack tip field becomes negligible. This specific radius is subsequently referred to as

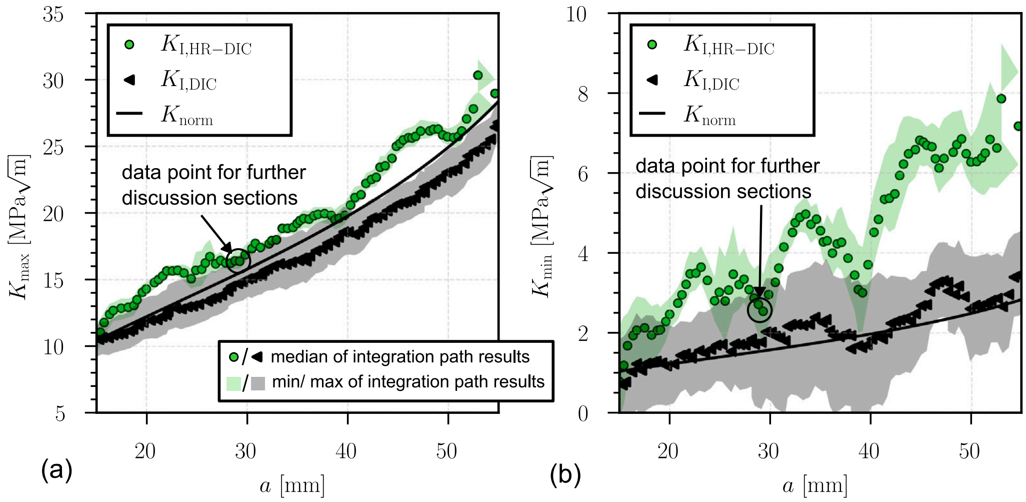

Fig. 7. Evolution of the maximum SIF $K_{\max}$ and minimum SIF $K_{\min}$ along the crack length compared to the analytical SIF solution according to ASTM E647-15 [29] (see Eq. (4)).

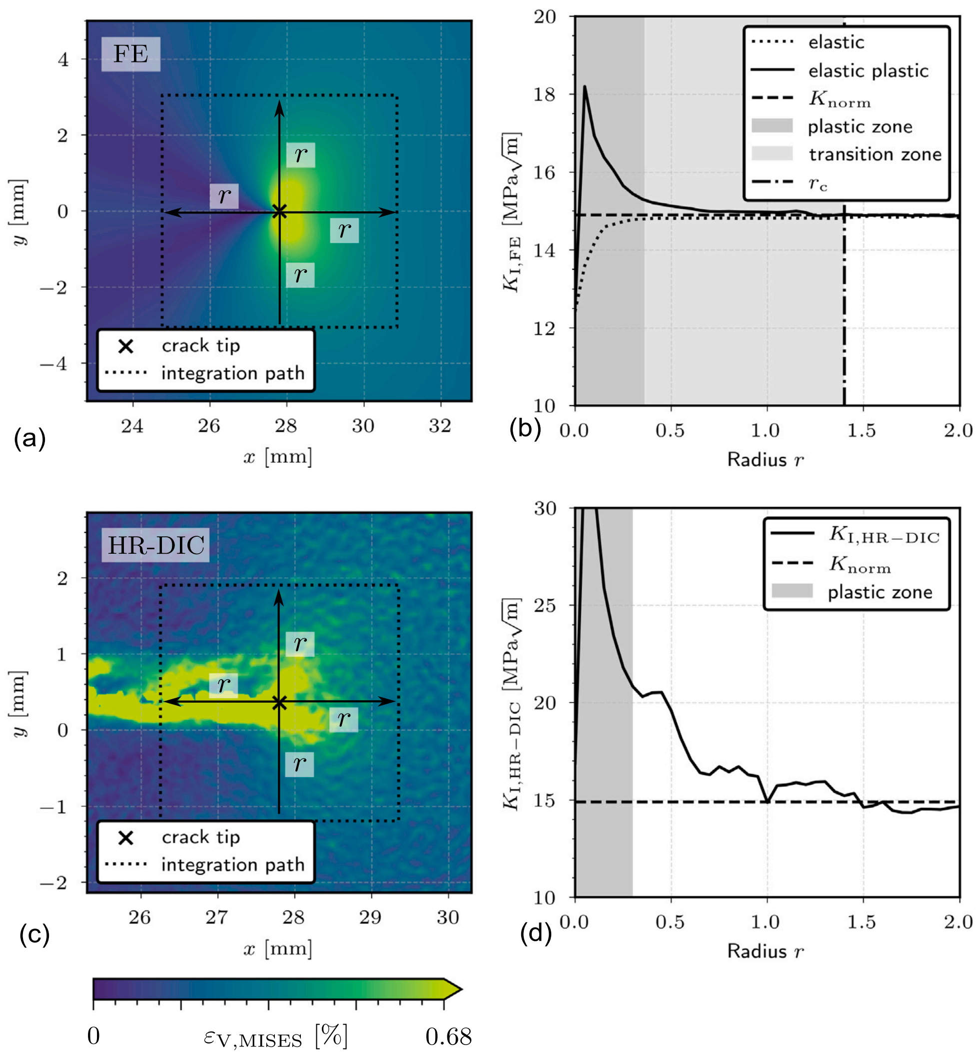

Fig. 8. Influence study analysing the impact of integration in close proximity of the PZ: (a) FE von MISES equivalent strain on the free surface of the elastic–plastic FE model, (b) $K_{\mathrm{I,FE}}$ path results for different r, (c) HR-DIC von MISES equivalent strain and (d) $K_{\mathrm{I,HR-DIC}}$ path results for different r; evaluated at $K_{\mathrm{norm}} = 14.9\,\mathrm{MPa}\sqrt{\mathrm{m}}$ and $a = 28\,\mathrm{mm}$.

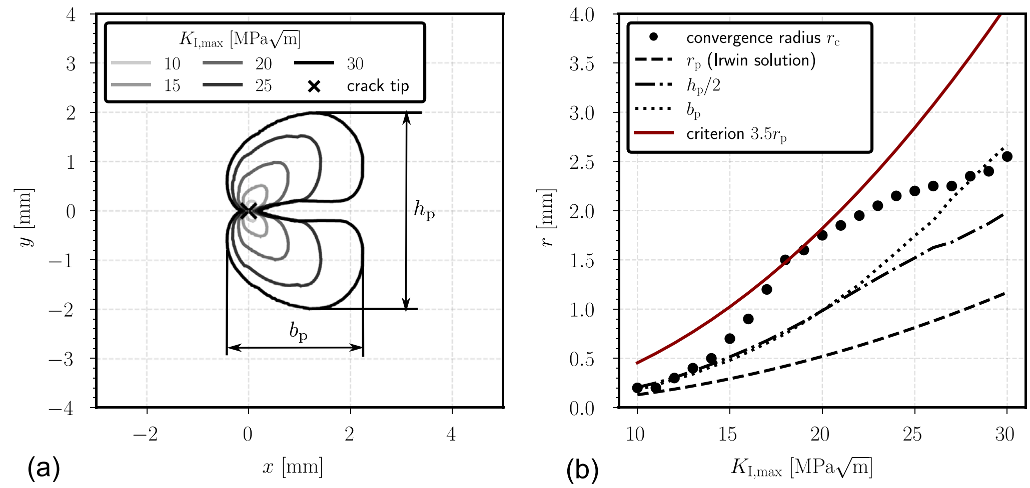

Fig. 9. The evolution of the convergence radius r_c in dependency of different maximum SIFs: (a) the dimension and shape of PZ at selected maximum SIFs and (b) height h_p and width b_p of the PZ compared to the r_c.

the convergence radius r_c. Due to the numerical scatter, the path results also fluctuate slightly in the converged region ($r > r_c$). The maximum path value of the last 50 integration path defines the boundary value. As shown in Fig. 8b the SIF results are overestimated in $r < r_c$. Coming from the left ($r = 0\,\text{mm}$) the first SIF results at radius r that intersects this boundary value, is considered as r_c. Fig. 9 investigates the dependency of r_c on different maximum SIFs. Therefore, in total 21 FE simulation with a maximum SIF range of $K_{max} = [10, 30]\,\text{MPa}\sqrt{\text{m}}$ were performed. At the end of each simulation, r_c is determined based on the nodal solution of the free surface of the 3D FE model.

Fig. 9 shows that r_c depends on the maximum SIF since it increases with increasing stress intensity. Furthermore, the results indicate that r_c is influenced by the shape of the PZ. From literature [11–13], it is known, that in thin sheet materials the wing shape of the PZ changes with increasing maximum SIF. This is referred to the increasing predominant plane stress condition within the sheet material. At a specific ratio between the thickness of the sheet and the maximum SIF, the wings of the PZ expand more in width than in height as exemplary shown in Fig. 9a for the configuration considered in this study. In case of this analysis, this turning point is reached at $K_{I,max} = 17\,\text{MPa}\sqrt{\text{m}}$ as shown in Fig. 9b. The shapes of the PZ at selected maximum SIF are given in Fig. 9a. Regarding r_c, the values exhibit a quadratic increasing behaviour until this turning point is reached. Afterwards, it increases almost parallel to the wing height of a single wing $h_p/2$.

It is therefore challenging to derive a general convergence criterion, given the numerous influences on the shape of PZ, including mixed-mode loading conditions, material and microstructure properties, and specimen thickness. To provide a conservative but robust estimate for use with the interaction integral on displacement field data of AA2024-T3, the authors have developed the following criterion:

$$r \geq 3.5 \cdot r_p = \frac{1.75}{\pi} \cdot \left(\frac{K_{I,max}}{\sigma_{yield}}\right)^2 \tag{6}$$

With satisfying this criterion, the influence of PZ on the SIF results can be neglected. However, this criterion is limited to 2 mm-thick sheet specimens made of AA2024-T3 subjected predominantly to mode I loading. Due to the limited measurement range of the HR-DIC data, a significant portion of the integration paths lies within the range $r_{p,ESZ} < r < r_c$ and, thus, $K_{I,HR-DIC}$ is overestimated. This effect is particularly evident in the K_{max} over a shown in Fig. 7a. There is a systematic offset between $K_{I,HR-DIC}$ and K_{norm} which increases slightly with increasing K_{max}. As the size of the PZ increases, the proportion of integration paths within the convergence range decreases, explaining this increased overestimation. Furthermore, comparing the distances between $K_{I,HR-DIC}$ and K_{norm} at maximum load (see Fig. 7a) and minimum load (see Fig. 7b) indicates that a load dependency exists. When the load is at its maximum, the elastic field around the crack tip is subject to a stronger influence, which in turn results in a more pronounced overestimation of $K_{I,HR-DIC}$ at the maximum load in comparison to the minimum load. This effect may be the reason why the HR-DIC FCP curve in Fig. 6 is slightly shifted to the right compared to the DIC curve.

3.3. The impact of plastic wake and the integration path gap

When applied to DIC displacement field data, closed line integrals are not feasible as the separation of material along the crack path results in erroneous displacement and strain calculations. These errors would distort the outcome of the interaction integrals. Furthermore, the HR-DIC system allows to resolve the plastic wake. Due to the locally varying crack path resulting from microscopic crack deflections and branching, it is often unavoidable, even with the integration path gap of Γ_o, that portions of the integration path extend into the plastically deformed region around the crack path. At these integration points, the stresses σ are therefore inaccurately calculated due to the underlying linear-elastic material model. In order to analyse the impact of the integration path gap as well as a likely integration within the plastic wake, FE simulations with and without crack propagation were conducted. Therefore, the Releasing-Constraint method from Section 2.2 is used. The elastic–plastic material model is identical to the one in Section 3.2. For integration, 10 integration paths are used with a distance of 0.05 mm to each other. The distances to each side of the rectangular integration path within the free surface von MISES equivalent strain field based on FE and HR-DIC are given in Fig. 10a and b. Regarding $K_{norm} = 14.9\,\text{MPa}\sqrt{\text{m}}$, all integration paths satisfy the convergence criterion from Eq. (6).

Fig. 10b shows the variation of $K_{I,FE}$ as a function of Γ_o. Both trends, with and without crack propagation calculation, align precisely from a qualitative perspective. This observation indicates that the result of $K_{I,FE}$ is not influenced by plastic wake. Instead, the study reveals sensitivity to the path gap Γ_o. For $\Gamma_o < 0.5\,\text{mm}$, K_I deviates by approximately 4 % from K_{norm}. The gradient of this decrease increases with the size of Γ_o. The comparison with the HR-DIC-based $K_{I,HR-DIC}$ evaluation exhibits a nearly identical characteristic. Due to the excellent agreement between the trends of the FE and HR-DIC analyses, this study recommends keeping Γ_o as small as possible. To ensure the applicability of Hooke's law as a material model, it is strongly advised to define the integration paths as close as possible to the plastic wake,

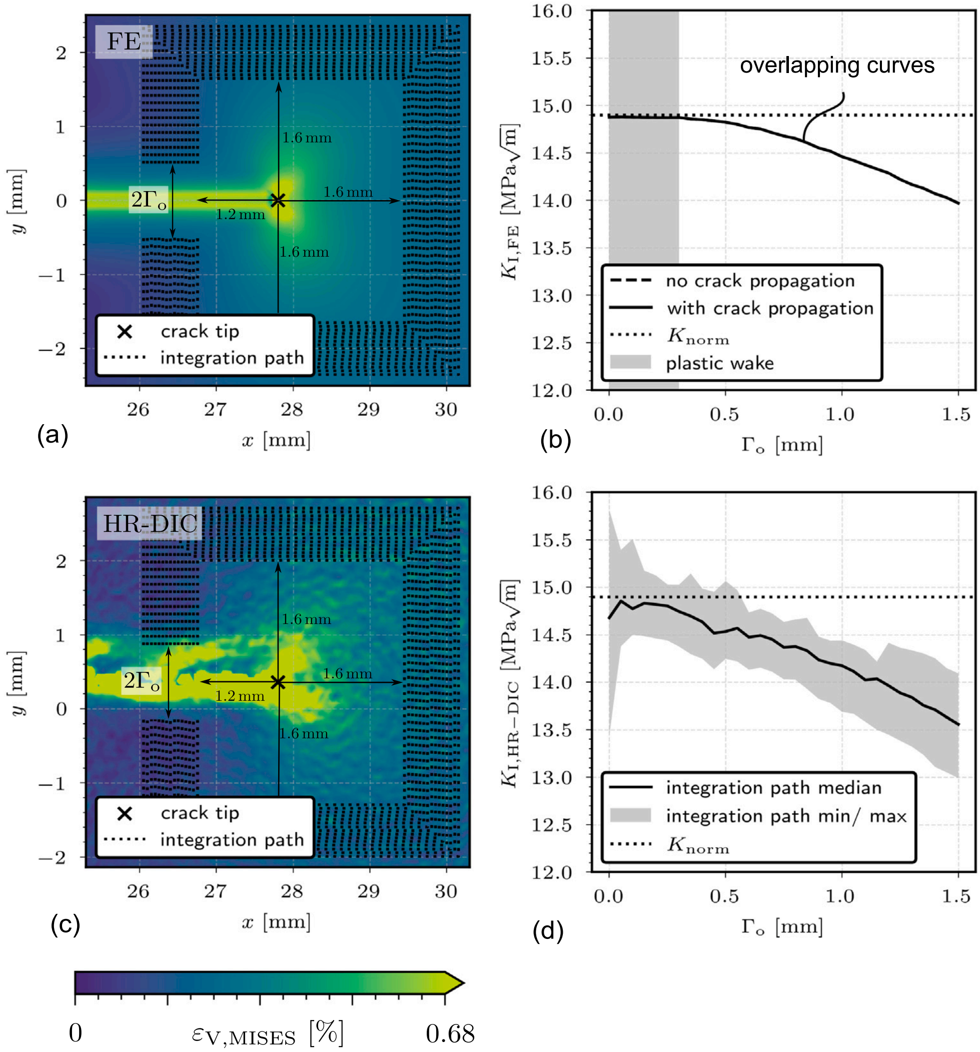

Fig. 10. Influence study analysing the impact of the integration path gap and integrating within the plastic wake: (a) FE von MISES equivalent strain field of the free surface of the FE model with crack propagation, (b) $K_{I,FE}$ path results for different integration path gaps Γ_0, (c) HR-DIC von MISES equivalent strain field and (d) $K_{I,HR-DIC}$ path results for different integration path gaps Γ_0; evaluated at $K_{norm} = 14.9\,\mathrm{MPa}\sqrt{\mathrm{m}}$ and $a = 28\,\mathrm{mm}$.

but within the elastic near-field. The analysis shows that even partial integration within the plastic wake results in a negligible deviation from K_{norm}, despite being theoretically inaccurate from a continuum mechanics perspective. The analysis of the scatter band indicates that variations in the integration path results significantly increase when integrating close to the crack path ($\Gamma_o = 0\,\mathrm{mm}$). For the application of the interaction integral with the given HR-DIC data, a minimum gap of $\Gamma_o > 0.2\,\mathrm{mm}$ is recommended. As K_{max} increases, the size of the integration path gap Γ_o also increases. Consequently, the proportion of the gap relative to the entire integration path increases, leading, as shown in Figs. 10b and d, to lower K_I values than those calculated by (4). This effect partially compensates for the overestimation of K_I due to the influence of the PZ and its transition zone at high K_{max}, resulting in HR-DIC-based FCP curves aligning closely with K_{norm} in the range $\Delta K > 15\,\mathrm{MPa}\sqrt{\mathrm{m}}$ in Fig. 6.

3.4. The crack closure effect

The original formulation of the interaction integral assumes crack flanks to be free of external loads. However, this assumption is no longer valid in the presence of crack closure. *Elber* [47] demonstrated that, during fatigue crack growth in AA2024-T3 at $R = 0.1$, plasticity-induced crack closure occurs. Moreover, several numerical studies [48–50] have shown that contact between the crack flanks primarily occurs at the free specimen surface. The contact pressure induces a residual stress field, which affects the application of the interaction integral at the surface. The question arises as to how crack face contact, resulting from crack closure mechanisms, influences the outcome of K_I. To address this, the elastic–plastic FE crack propagation simulation from the previous study is extended to include the contact definition by using contact elements. The evaluation of $K_{I,FE}$ is based on the nodal displacements of the specimen surface. To isolate the effect of crack face contact from other influences discussed in previous sections, $K_{I,FE}$ is determined both with and without the contact definition. For the simulation without contact definition the rigid target surface as well as all contact elements are deleted, allowing the crack faces of the MT-160 model to deform freely. This approach allows for a targeted investigation of the influence of crack face contact and the resulting elastic residual stress field near the crack path. The results are compared with the HR-DIC-based evaluation of $K_{I,HR-DIC}$. For this purpose, $K_{I,HR-DIC}$ is determined at each of the 30 load steps during crack opening. The HR-DIC data are derived from the load cycle recording at $a = 27.8\,\mathrm{mm}$. The location of the ten integration paths is identical in both the FE and HR-DIC data, as shown in Figs. 11a and c.

Fig. 11b compares the $K_{I,FE}$ trends based on FE data with and without the contact definition. The results indicate that crack face

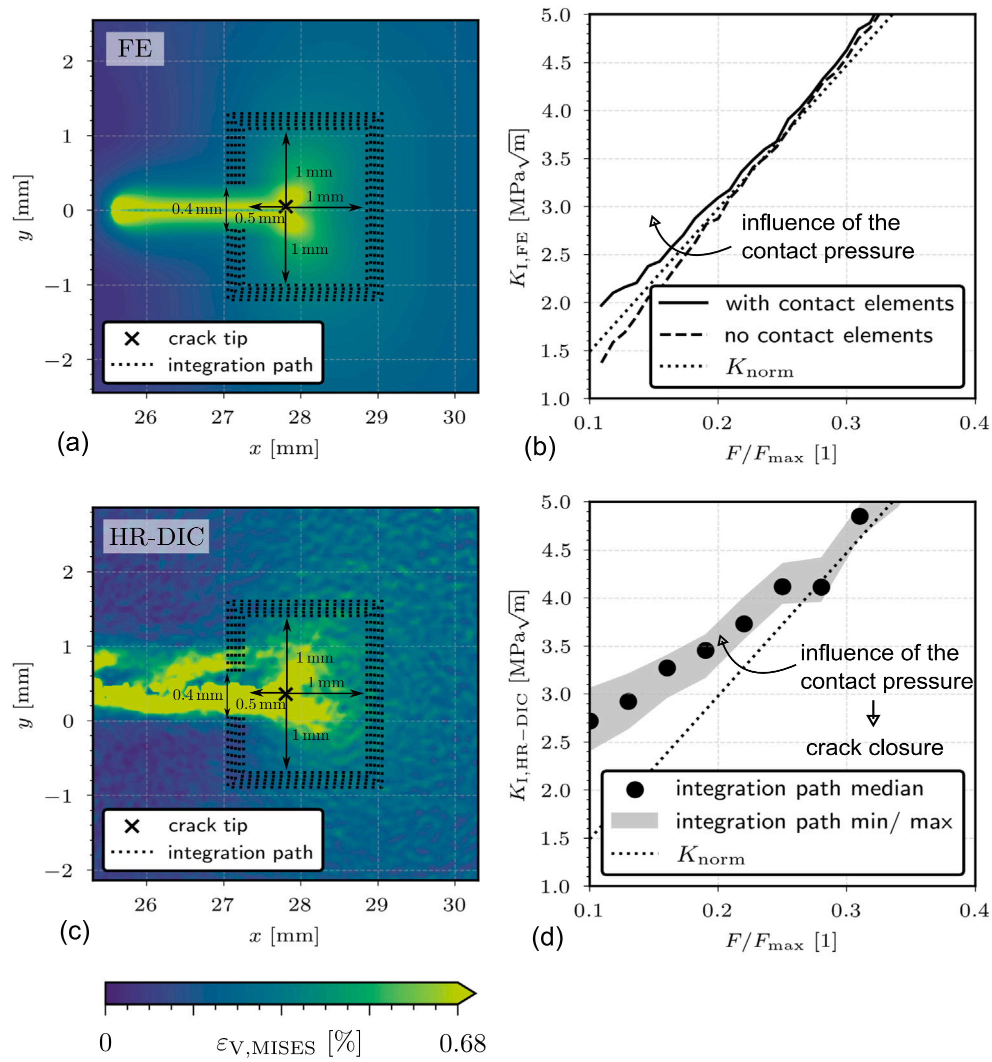

Fig. 11. Influence study analysing the impact of crack face contact due to crack closure: (a) FE von MISES equivalent strain field of the free surface of the FE model, (b) $K_{\mathrm{I,FE}}$ as a function of the load F comparing a FE simulation with and without contact definition, (c) HR-DIC von MISES equivalent strain field and (d) $K_{\mathrm{I,HR-DIC}}$ along the crack opening load F; evaluated at $K_{\mathrm{norm}} = 14.9\,\mathrm{MPa}\sqrt{\mathrm{m}}$ and $a = 28\,\mathrm{mm}$.

Table 4
$K_{\mathrm{I,FE,min}}$ results of the single integration paths evaluated on displacement field data of the free surface of the 3d FE model at minimum load $K_{\mathrm{norm}} = 1.49\,\mathrm{MPa}\sqrt{\mathrm{m}}$; integration path #1 denotes the path that is closest to the crack tip.

Integration path	$K_{\mathrm{I,FE,min}}$ without contact	$K_{\mathrm{I,FE,min}}$ with contact
#1	$0.69\,\mathrm{MPa}\sqrt{\mathrm{m}}$	$1.53\,\mathrm{MPa}\sqrt{\mathrm{m}}$
#2	$1.14\,\mathrm{MPa}\sqrt{\mathrm{m}}$	$1.81\,\mathrm{MPa}\sqrt{\mathrm{m}}$
#3	$1.37\,\mathrm{MPa}\sqrt{\mathrm{m}}$	$1.97\,\mathrm{MPa}\sqrt{\mathrm{m}}$
#4	$1.64\,\mathrm{MPa}\sqrt{\mathrm{m}}$	$2.16\,\mathrm{MPa}\sqrt{\mathrm{m}}$
#5	$1.86\,\mathrm{MPa}\sqrt{\mathrm{m}}$	$2.36\,\mathrm{MPa}\sqrt{\mathrm{m}}$

contact leads to an increase in $K_{\mathrm{I,FE}}$ compared to K_{norm} near minimum load. This behaviour is not observed in the $K_{\mathrm{I,FE}}$ trend without the contact definition, suggesting that crack face contact results in an slightly increased $K_{\mathrm{I,FE}}$. The comparison with the HR-DIC-based evaluation of $K_{\mathrm{I,HR-DIC}}$ shows a similar trend, consistent with the findings of J-integral studies by *Gonzales et al.* [25]. The main difference is that the deviation from the K_{norm} reference line is more pronounced. This is also evident in the comparison of K_{I} values at minimum load $F_{\min}$. Specifically, $K_{\mathrm{I,FE,min}} = 2\,\mathrm{MPa}\sqrt{\mathrm{m}}$ is lower than $K_{\mathrm{I,HR-DIC,min}} = 2.74\,\mathrm{MPa}\sqrt{\mathrm{m}}$. This difference is attributed to the significantly higher contact pressure between the two crack faces. Compared to the FE crack propagation simulation, the actual crack growth increment per load cycle is much smaller than $\Delta a = 0.05\,\mathrm{mm}$. Consequently, the accumulation of plastic strain within the PZ is substantially increased for propagating fatigue cracks in AA2024-T3, which also results in larger contact pressures between the crack faces. Furthermore, isotropic hardening is employed instead of kinematic hardening to ensure a more robust numerical simulation. However, when considering the cyclic deformation behaviour at the crack tip of a real fatigue crack, the kinematic hardening components of the cyclic material response of AA2024-T3 would be expected to further increase plastic deformation along the crack path, ultimately leading to higher crack face contact pressures. Furthermore, the good agreement between the FE-based analysis and the HR-DIC data-based evaluation suggests that the predominant crack closure mechanism is plasticity-induced crack closure. This conclusion is based on the fact that the FE model is only capable of representing this specific closure mechanism. Furthermore, Table 4 indicates that the crack closure contact does not lead to an increase in path dependency. The difference values between the successive single-path results are almost all of a similar order of magnitude. A noticeable decrease in the path results can be observed with increasing

Table 5
Comparison between $K_{\mathrm{I,min}}$ from FE and HR-DIC displacement field data and the actual crack opening loads $K_{\mathrm{op,ctod}}$ (see [51]); $K_{\mathrm{I,min}}$ represents the median of the path results.

SIF	FE	HR-DIC
$K_{\mathrm{op,ctod}}$ $\mathrm{MPa}\sqrt{\mathrm{m}}$	6.63	7.42
$K_{\mathrm{I,min}}$ $\mathrm{MPa}\sqrt{\mathrm{m}}$	1.97	2.66

proximity to the crack tip, as evident in both simulations with and without contact definition. This behaviour can be attributed to the deformation behaviour of the plastic wake while crack propagation is performed. According to Elber's explanation [47], material flow occurs into the crack plane during crack propagation. Consequently, in the FE model, even under a loading ratio of $R = 0.1$, nodes located near the crack plane exhibit negative displacements, which produce this effect upon numerical integration. The introduction of a contact definition counteracts this behaviour to some extent but does not eliminate it completely, since contact penetration is permitted by the augmented Lagrange contact formulation. The influence of this effect decreases with increasing integration distance from the crack tip. Hence, it can be concluded that this phenomenon arises primarily due to the proximity to the crack tip and the FE modelling assumptions used in this work.

Although the cause of the SIF overestimation is strongly suggested by the good agreement between the trends observed in the HR-DIC- and FE-based evaluations, small secondary cracks located behind the crack tip may also influence the stress intensity factor at minimum load. In addition, the slight asymmetry of the near-crack-tip field observed in Fig. 11c indicates minor mixed-mode loading conditions at the specimen surface, which may slightly affect the SIF evaluation using the interaction integral method. In contrast, roughness-induced and oxide-induced crack closure are not expected to play a significant role. While the crack growth behaviour investigated experimentally in this study predominantly lies within the Paris regime, both mechanisms are known to occur mainly in AA2024-T3 in the threshold regime. Furthermore, no specific environmental conditions are present that would particularly promote oxide-induced crack closure.

The authors investigated the crack closure behaviour of the identical crack tip and specimen in a previous study using local COD measurements to analyse the crack opening kinematics [51]. Therefore, the K_{op} values along the crack front for the same numerical model presented in Section 2.2 and the same HR-DIC measurements were investigated. $K_{\mathrm{op,ctod}}$ denotes the first crack tip stress at which no contact between the crack faces close behind the crack tip exists during crack opening. Table 5 presents the $K_{\mathrm{op,ctod}}$ values for the FE and HR-DIC investigation from the previous experimental HR-DIC work [51].

Table 5 points out that the actual crack opening loads are significant higher, indicating that $K_{\mathrm{I,min}}$ derived by the interaction integral from displacement field data does not represent the crack opening load $K_{\mathrm{op,ctod}}$. However, the previous results showed that crack closure increases slightly the SIF value which causes additionally the increasing character of the $K_{\mathrm{I,HR-DIC}}$ trend along the crack length at minimum load from Fig. 7b.

4. Conclusions

In this paper, the authors investigate the applicability of the interaction integral for determining SIFs within high-resolution displacement field data. Given the aim of the fracture mechanics community to obtain multi-scale time-series data that bridges the gap between local microscopic fatigue crack growth mechanisms and their impact on the macroscopic fatigue crack growth behaviour represented by the FCP curve, this paper identifies influences and analyses their impact on the interaction integral. In particular, the following conclusions are drawn:

- HR-DIC and DIC-based crack propagation curves, developed using the new methodology, accurately reflect the crack growth behaviour similar to the established ASTM E647-15 [29] method. This is demonstrated by their agreement within a common scatter band and is quantitatively supported by high $R^2 > 0.95$ values, as shown in the comparison of the respective crack growth curves.
- Integrating near the PZ results likely in an overestimation of the SIF. Furthermore, a dependency of the convergence radius on the shape of the PZ is identified. The convergence radius describes the minimum distance between the integration path and the crack tip, and for consistent results, a conservative estimate can be obtained by using the condition $r \geq 7/2 \cdot r_{\mathrm{p}}$, where r_{p} is the PZ size. This criterion is limited to AA2024-T3 and a 2 mm sheet specimen under predominant mode-I loading.
- The size of the path gap around the crack path relative to the total integration path length significantly impacts the interaction integral results. The results indicate that larger gaps lead to smaller values. It is recommended to keep the exclusion gap as small as possible. Integrating close to the crack path increases the scatter between different integration paths pointing towards a loss in path independence. However, this seems to have a negligible effect on the mean result, provided the integration paths remain within the elastic field near the PZ.
- Crack face contact seems to increase the interaction integral results, but the values remain significantly lower than the measured K_{op} values. Moreover, the results indicate that crack face does not contribute to an increased loss of path independence.

The present study places the application of the interaction integral at the centre of the analysis and examines its use in combination with HR-DIC data for the determination of crack-tip loading conditions. These quantities form a crucial basis for reliable lifetime assessments of engineering components containing cracks. A systematic analytical separation of the individual influencing effects and a detailed understanding of their cause–effect relationships within the interaction integral framework remain open issues and offer significant potential for future research.

CRediT authorship contribution statement

Florian Paysan: Writing – original draft, Methodology, Investigation, Formal analysis, Data curation, Conceptualization. **David Melching:** Writing – review & editing, Software, Investigation. **Eric Breitbarth:** Writing – review & editing, Supervision, Software, Funding acquisition, Conceptualization.

Declaration of competing interest

The authors declare that they have no known competing financial interests or personal relationships that could have appeared to influence the work reported in this paper.

Acknowledgements

The authors acknowledge the financial support of the DLR-Directo rate Aeronautics. This work was supported by the Deutsche Forschungsgemeinschaft, Germany (DFG) via the project Experimental analysis and phase-field modelling of the interaction between PZ and fatigue crack growth in ductile materials under complex loading (grant number BR 6259/2-2). Furthermore, funding came from the Federal Ministry for Economic Affairs and Climate Action, Germany on the basis of a decision by the German Bundestag, within the framework of the aerospace program LuFo-VI of the project "Intelligent FSW Process Monitoring" (Funding ID 20W2201E).

Data availability

Data will be made available on request.

References

[1] J. Schijve, Fatigue damage in aircraft structures, not wanted, but tolerated? Int. J. Fatigue (31) (2009) 998–1011, http://dx.doi.org/10.1016/j.ijfatigue.2008.05.016.

[2] R.O. Ritchie, Mechanisms of fatigue-crack propagation in ductile and brittle solids, Int. J. Fract. (100) (1999) 55–83, http://dx.doi.org/10.1023/A:1018655917051.

[3] R. Jones, Fatigue crack growth and damage tolerance, Fatigue Fract. Eng. Mater. Struct. 37 (5) (2014) 463–483, http://dx.doi.org/10.1111/ffe.12155.

[4] P. Chowdhury, H. Sehitoglu, Mechanisms of fatigue crack growth - a critical digest of theoretical developments, Fatigue Fract. Eng. Mater. Struct. 39 (6) (2016) 652–674, http://dx.doi.org/10.1111/ffe.12392.

[5] D. Camas, P. Lopez-Crespo, A. Gonzalez-Herrera, B. Moreno, Numerical and experimental study of the plastic zone in cracked specimens, Eng. Fract. Mech. 185 (2017) 20–32, http://dx.doi.org/10.1016/j.engfracmech.2017.02.016.

[6] D. Camas, J. Garcia-Manrique, A. Gonzalez-Herrera, Crack front curvature: Influence and effects on the crack tip fields in bi-dimensional specimens, Int. J. Fatigue 44 (2012) 41–50, http://dx.doi.org/10.1016/j.ijfatigue.2012.05.012.

[7] Camas, J. Garcia-Manrique, A. Gonzalez-Herrera, Numerical study of the thickness transition in bi-dimensional specimen cracks, 33, (921–928) 2011, http://dx.doi.org/10.1016/j.ijfatigue.2011.02.006.

[8] J. Garcia-Manrique, D. Camas, P. Lopez-Crespo, A. Gonzalez-Herrera, Stress intensity factor analysis of through thickness effects, Int. J. Fatigue 46 (2013) 58–66, http://dx.doi.org/10.1016/j.ijfatigue.2011.12.012.

[9] A. Gonzalez-Herrera, J. Zapatero, Tri-dimensional numerical modelling of plasticity-induced fatigue crack closure, Eng. Fract. Mech. (75) (2008) 4513–4528, http://dx.doi.org/10.1016/j.engfracmech.2008.04.024.

[10] D.S. Dugdale, Yielding of steel sheets containing slits, J. Mech. Phys. Solids 8 (1959) 100–104, http://dx.doi.org/10.1016/0022-5096(60)90013-2.

[11] M. Besel, E. Breitbarth, Advanced analysis of crack tip plastic zone under cyclic loading, Int. J. Fatigue 93 (2016) 92–108, http://dx.doi.org/10.1016/j.ijfatigue.2016.08.013.

[12] F. Caputo, G. Lamanna, A. Soprano, On the evaluation of the plastic zone size at the crack tip, Eng. Fract. Mech. 103 (2013) 162–173, http://dx.doi.org/10.1016/j.engfracmech.2012.09.030.

[13] R. Gadallah, H. Murakawa, K. Ikushima, M. Shibahara, S. Tsutsumi, Numerical investigation on the effect of thickness and stress level on fatigue crack growth in notched specimens, Theor. Appl. Fract. Mech. 116 (2021) 103138, http://dx.doi.org/10.1016/j.tafmec.2021.103138.

[14] J.D. Carroll, W. Abuzaid, J. Lambros, H. Sehitoglu, High resolution digital image correlation measurements of strain accumulation in fatigue crack growth, Int. J. Fatigue 57 (2013) 140–150, http://dx.doi.org/10.1016/j.ijfatigue.2012.06.010.

[15] W. Zhang, L. Cai, D. Zhou, F. Sun, In-situ microscopy testing of plasticity variation ahead of fatigue crack tip in AL2024-T3, Int. J. Fract. 216 (1) (2019) 59–70, http://dx.doi.org/10.1007/s10704-018-00340-y, PII: 340.

[16] J.M. Vasco-Olmo, F.A. Díaz, M.N. James, B. Yang, Crack tip plastic zone evolution during an overload cycle and the contribution of plasticity–induced shielding to crack growth rate changes, Fatigue Fract. Eng. Mater. Struct. 41 (2018) 2172–2186, http://dx.doi.org/10.1111/ffe.12840.

[17] N. Gehri, J. Mata-Falcón, W. Kaufmann, Automated crack detection and measurement based on digital image correlation, Constr. Build. Mater. 256 (2020) 119383, http://dx.doi.org/10.1016/j.conbuildmat.2020.119383.

[18] J. Réthoré, Automatic crack tip detection and stress intensity factors estimation of curved cracks from digital images, Internat. J. Numer. Methods Engrg. 103 (2015) 516–534, http://dx.doi.org/10.1002/nme.4905.

[19] D. Melching, F. Paysan, T. Strohmann, E. Breitbarth, An iterative crack tip correction algorithm discovered by physical deep symbolic regression, Int. J. Fatigue 187 (2024) 108432, http://dx.doi.org/10.1016/j.ijfatigue.2024.108432.

[20] T. Strohmann, D.-P. Penner, E. Breitbarth, G. Requena, Automatic detection of fatigue crack paths using digital image correlation and convolutional neural networks, Fatigue Fract. Eng. Mater. Struct. 44 (2021) 1336–1348, http://dx.doi.org/10.1111/ffe.13433.

[21] D. Melching, T. Strohmann, G. Requena, E. Breitbarth, Explainable machine learning for precise fatigue crack tip detection, Sci. Rep. 12 (1) (2022) 9513, http://dx.doi.org/10.1038/s41598-022-13275-1.

[22] C. Zhang, M. Lei, Y. Chen, B. Kuang, S. Liu, Y. Ding, Q. Fang, X. Li, W. He, H. Xie, Automatic crack tip localization in enormous DIC images to in-situ characterize high-temperature fatigue crack growth behavior, Int. J. Fatigue (ISSN: 01421123) 185 (2024) 108364, http://dx.doi.org/10.1016/j.ijfatigue.2024.108364, URL https://linkinghub.elsevier.com/retrieve/pii/S0142112324002226.

[23] X. Sun, L. Huang, J. Li, Z. Xia, Y. Ding, Q. Fang, B. Liu, W. He, H. Xie, Intelligent localization method of fatigue crack tips in enormous high-temperature DIC images, Opt. Laser Technol. (ISSN: 00303992) 186 (2025) 112666, http://dx.doi.org/10.1016/j.optlastec.2025.112666, URL https://linkinghub.elsevier.com/retrieve/pii/S0030399225002543.

[24] H. Zheng, Y. Ding, S. Liu, M.Z. Rahimi, X. Sun, H. Luo, W. He, H. Xie, R. Zhao, Automatic high-precision fatigue crack tip localization without empirical parameters in enormous DIC datasets of GH4169 superalloy served under extreme environments, Theor. Appl. Fract. Mech. (ISSN: 01678442) 140 (2025) 105144, http://dx.doi.org/10.1016/j.tafmec.2025.105144, URL https://linkinghub.elsevier.com/retrieve/pii/S0167844225003027.

[25] G.L. Gonzáles, J.A. González, J.T. Castro, J.L. Freire, A J-integral approach using digital image correlation for evaluating stress intensity factors in fatigue cracks with closure effects, Theor. Appl. Fract. Mech. 90 (2017) 14–21, http://dx.doi.org/10.1016/j.tafmec.2017.02.008.

[26] E. Breitbarth, T. Strohmann, M. Besel, S. Reh, Determination of stress intensity factors and J integral based on digital image correlation, Frat. Integrità Strutt. 13 (49) (2019) 12–25, http://dx.doi.org/10.3221/IGF-ESIS.49.02.

[27] M.R. Molteno, T.H. Becker, Mode I–III decomposition of the J-integral from DIC displacement data, Strain 51 (492–503) (2015) http://dx.doi.org/10.1111/str.12166.

[28] J. Rethore, A. Gravouil, F. Morestin, A. Combescure, Estimation of mixed-mode stress intensity factors using digital image correlation and an interaction integral, Int. J. Fract. 132 (1) (2005) 65–79, http://dx.doi.org/10.1007/s10704-004-8141-4.

[29] ASTM (Ed.), ASTM E647-15 Standard Test Method for Measurement of Fatigue Crack Growth Rates. http://dx.doi.org/10.1520/E0647-15.

[30] M. Stern, E.B. Becker, R.S. Dunham, A contour integral computation of mixed-mode stress intensity factors, Int. J. Fract. (12) (1976) 359–368, http://dx.doi.org/10.1007/BF00032831.

[31] J.F. Yau, S.S. Wang, H.T. Corten, A mixed-mode crack analysis of isotropic solids using conservation laws of elasticity, J. Appl. Mech. (47) (1980) 335–341, http://dx.doi.org/10.1115/1.3153665.

[32] M. Xu, Y. Liu, H. Yuan, Characterization of crack-tip fields for elastoplastic fatigue crack growth part I: Analysis of the ΔJ-integral, Eng. Fract. Mech. (275) (2022) 108847, http://dx.doi.org/10.1016/j.engfracmech.2022.108847.

[33] T. Strohmann, D. Melching, F. Paysan, A. Klein, E. Dietrich, G. Requena, E. Breitbarth, Crack analysis tool in python - crackpy (2022), 2022, http://dx.doi.org/10.5281/zenodo.7319653, URL https://github.com/dlr-wf/crackpy.

[34] F. Paysan, E. Breitbarth, Towards three dimensional aspects of plasticity-induced crack closure: A finite element simulation, Int. J. Fatigue 163 (2022) 107092, http://dx.doi.org/10.1016/j.ijfatigue.2022.107092.

[35] Tamarin, Atlas of Stress-Strain Curves, second ed., ASM International, Materials Park, Ohio, ISBN: 978-0-87170-739-0, 2002.

[36] F.V. Antunes, D.M. Rodrigues, Numerical simulation of plasticity induced crack closure: Indentification and discussion of parameters, Eng. Fract. Mech. 75 (2008) 3101–3120, http://dx.doi.org/10.1016/j.engfracmech.2007.12.009.

[37] S. Pommier, P. Bompard, Bauschinger effect of alloys and plasticity–induced crack closure: a finite element analysis, Fatigue Fract. Eng. Mater. Struct. 23 (2001) 129–139, http://dx.doi.org/10.1046/j.1460-2695.2000.00259.x.

[38] S. Pommier, A study of the relationship between variable level fatigue crack growth and the cyclic constitutive behaviour of steel, Int. J. Fatigue 23 (2001) 111–118, http://dx.doi.org/10.1016/S0142-1123(01)00165-7.

[39] D. Camas, F. Antunes, B. Moreno, A. Gonzalez-Herrera, Numerical analysis of the influence of the last cycle scheme on plasticity induced crack closure, Procedia Struct. Integr. 17 (2019) 894–899, http://dx.doi.org/10.1016/j.prostr.2019.08.119.

[40] D. Camas, J. Garcia-Manrique, F.V. Antunes, A. Gonzalez-Herrera, Three-dimensional fatigue crack closure numerical modelling: Crack growth scheme, Theor. Appl. Fract. Mech. 108 (2020) 102623, http://dx.doi.org/10.1016/j.tafmec.2020.102623.

[41] C. Laird, R. de La Veaux, Additional evidence for the plastic blunting process of fatigue crack propagation, Met. Trans. A (8) (1977) 657–664, http://dx.doi.org/10.1007/BF02676989.

[42] F. Paysan, E. Dietrich, E. Breitbarth, A robot-assisted microscopy system for digital image correlation in fatigue crack growth testing, Exp. Mech. (2023) http://dx.doi.org/10.1007/s11340-023-00964-9.

[43] GOM, Gom aramis 2020 version 2, 2020.

[44] F. Bergner, G. Zouhar, G. Tempus, The material-dependent variability of fatigue crack growth rates of aluminium alloys in the Paris regime, Int. J. Fatigue 23 (2001) 383–394, http://dx.doi.org/10.1016/S0142-1123(01)00006-8.

[45] M. Xu, Y. Liu, H. Yuan, On ΔJ characterization of elastic–plastic crack-tip fields under fatigue loading conditions, Int. J. Fatigue 160 (2022) 106849, http://dx.doi.org/10.1016/j.ijfatigue.2022.106849, URL https://www.sciencedirect.com/science/article/pii/S0142112322001244.

[46] D. Carka, C.M. Landis, On the path-dependence of the J-integral near a stationary crack in an elastic-plastic material, J. Appl. Mech. 78 (1) (2011) http://dx.doi.org/10.1115/1.4001748.

[47] W. Elber, Fatigue crack closure under cyclic tension, Eng. Fract. Mech. (2) (1970) 230–242, http://dx.doi.org/10.1016/0013-7944(70)90028-7.

[48] F.V. Antunes, L. Paiva, R. Branco, L.P. Borrego, Effect of underloads on plasticity-induced crack closure: A numerical analysis, J. Eng. Mater. Technol. 141 (3) (2019) http://dx.doi.org/10.1115/1.4042865.
[49] K. Masuda, S. Ishihara, N. Oguma, Effect of specimen thickness and stress intensity factor range on plasticity-induced fatigue crack closure in A7075-T6 alloy, Mater. (Basel, Switzerland) 14 (3) (2021) http://dx.doi.org/10.3390/ma14030664.
[50] T. Oplt, T. Vojtek, R. Kubíček, P. Pokorný, P. Hutař, Numerical modelling of fatigue crack closure and its implication on crack front curvature using $\Delta CTODp$, Int. J. Fatigue (2023) 107570, http://dx.doi.org/10.1016/j.ijfatigue.2023.107570.
[51] F. Paysan, D. Melching, E. Breitbarth, Plasticity-induced crack closure identification during fatigue crack growth in AA2024-T3 by using high-resolution digital image correlation, Int. J. Fatigue (ISSN: 01421123) 192 (2025) 108703, http://dx.doi.org/10.1016/j.ijfatigue.2024.108703, URL https://linkinghub.elsevier.com/retrieve/pii/S0142112324005620.